Line-of-Sight Observables Algorithms for the *Helioseismic and Magnetic Imager* (HMI) Instrument Tested with *Interferometric Bidimensional Spectrometer* (IBIS) Observations

**Sébastien Couvidat · S.P. Rajaguru · Richard Wachter ·
K. Sankarasubramanian · Jesper Schou ·
Philip H. Scherrer**

Abstract The *Helioseismic and Magnetic Imager* (HMI) instrument onboard the *Solar Dynamics Observatory* produces line-of-sight (LOS) observables (Doppler velocity, magnetic-field strength, Fe I line width, line depth, and continuum intensity) as well as vector magnetic-field maps at the solar surface. The accuracy of LOS observables is dependent on the algorithm used to translate a sequence of HMI filtergrams into the corresponding observables. Using one hour of high-cadence imaging spectropolarimetric observations of a sunspot in the Fe I line at 6173 Å through the *Interferometric Bidimensional Spectrometer* installed at the Dunn Solar Telescope, and the Milne–Eddington inversion of the corresponding Stokes vectors, we test the accuracy of the observables algorithm currently implemented in the HMI data-analysis pipeline: the MDI-like algorithm. In an attempt to improve the accuracy of HMI observables, we also compare this algorithm to others that may be implemented in the future: a least-squares fit with a Gaussian profile, a least-squares fit with a Voigt profile, and the use of second Fourier coefficients in the MDI-like algorithm.

Keywords Sun: helioseismology · Instrument: SDO/HMI, IBIS

1. Introduction

The *Helioseismic and Magnetic Imager* instrument (HMI: Schou *et al.*, 2012) onboard the *Solar Dynamics Observatory* satellite (SDO) makes measurements, in the Fe I absorption line centered at the in-air wavelength 6173.3433 Å (*e.g.*, Dravins, Lindegren, and Nordlund, 1981; Norton *et al.*, 2006), of the motion of the solar photosphere to study solar oscillations,

S. Couvidat (✉) · R. Wachter · J. Schou · P.H. Scherrer
W.W. Hansen Experimental Physics Laboratory, Stanford University, Stanford, CA, USA
e-mail: couvidat@stanford.edu

S.P. Rajaguru · K. Sankarasubramanian
Indian Institute of Astrophysics, Bengaluru, India

K. Sankarasubramanian
Space Astronomy Group, ISRO Satellite Centre, Bengaluru, India

and of the polarization to study all three components of the photospheric magnetic-field. HMI samples the neutral iron line at six positions (wavelengths) symmetrical around the line center at rest. The line-of-sight (LOS) observables, produced every 45 seconds, are Doppler velocity at the solar surface, LOS magnetic-field strength, and Fe I line width, line depth, and continuum intensity. They are calculated using 12 filtergrams: images taken at six wavelengths and two polarizations (left-circular and right-circular polarizations, here-after LCP and RCP). Unlike the *Michelson Doppler Imager* (MDI) instrument (Scherrer *et al.*, 1995), on which HMI is based, the observables calculations are performed on the ground, not onboard the satellite. This allows for more flexibility regarding which algorithm to apply, and makes reprocessing possible in the eventuality that a better algorithm is later implemented.

On 8 June 2007, the sunspot NOAA AR 10960 was observed by the *Interferometric Bidimensional Spectrometer* (IBIS) instrument (Cavallini, 2006) installed at the Dunn Solar Telescope of the National Solar Observatory at Sacramento Peak (New Mexico, USA). The full Stokes profile (*I*, *Q*, *U*, and *V*) of the Fe I line was scanned and imaged for seven hours at a cadence of 47.5 seconds, close to the HMI cadence (see Rajaguru *et al.*, 2010, for details on the IBIS data processing and calibration). The IBIS images have a spectral resolution of ≈ 25 mÅ and an image scale of $0.165''$ per pixel (both three times better than HMI), and the Fe I line was sampled at 23 different wavelengths spanning ≈ 900 mÅ. We select the first observation hour, to keep only the best seeing interval and to match the time interval selected for the Milne–Eddington inversion of the Stokes vectors (inversion following the method described by Skumanich and Lites (1987)).

The IBIS observations present some advantages over the HMI observations resulting from the higher number of wavelength samples. The line profiles can be interpolated at each pixel on a finer wavelength grid: simulations of HMI intensities can therefore be obtained by applying the filter transmission profiles to these wavelength-interpolated lines, and the accuracy of the LOS observables returned by the MDI-like algorithm can be investigated. Other algorithms can also be studied, such as a least-squares fit with an appropriate Fe I profile. Moreover, the Sun–Earth radial velocity varied little during the IBIS observation timespan (from -120.98 m s^{-1} to -95.43 m s^{-1} during the first observation hour, compared to a 358 m s^{-1} change for the HMI–Sun radial velocity over the same time interval on 8 June 2011). Another consideration for using IBIS data and their Milne–Eddington inversion is that, at the time of writing, the full Stokes vector inversions of HMI have not yet been officially released: the inversion code (vfisv: Borrero *et al.*, 2010) is still being fine-tuned. However, IBIS spatial resolution is different from HMI, a fact that must be factored in when interpreting the results: mainly due to convective blueshift (depending on how well granules are resolved), a different spatial resolution translates into a different Fe I line profile. In Section 2 we describe the MDI-like algorithm implemented in the HMI pipeline, in Section 3 we describe other algorithms tested, and in Section 4 we introduce the IBIS data used. We present the results in Section 5, and we conclude in Section 6.

2. MDI-Like Algorithm

This algorithm, based on what was implemented for the SOHO/MDI instrument, combines filtergrams taken at six wavelengths. The profiles of the corresponding HMI filter transmit-tances must be accurately known. The HMI optical filter system is composed of a front window, a blocking filter, a five-stage Lyot filter, and two Michelson interferometers. The Lyot element E1 (element with the lowest FWHM) and the two interferometers are tunable,

Figure 1 Example of HMI filter transmission profiles obtained from calibration procedures (from Couvidat *et al.*, 2012). Six tuning positions are shown with respect to the Fe I solar line (black line) at disk center and at rest, on top of a continuum tuning position (dashed line). The Fe I line profile was provided by R.K. Ulrich (private communication, 2011) and obtained at the Mount Wilson Observatory.
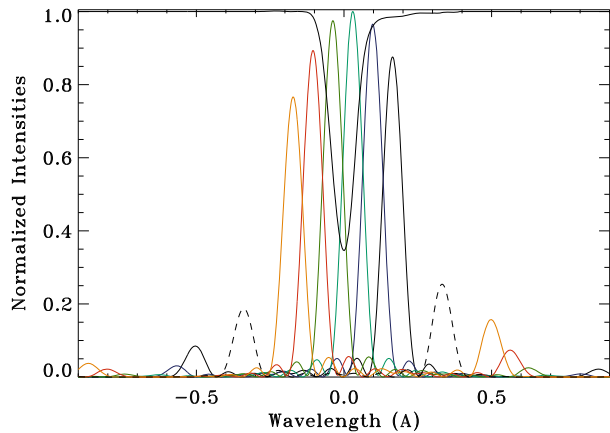
allowing one to obtain filtergrams at different wavelengths. The calculation of the resulting transmission profiles is detailed by Couvidat *et al.* (2012). An example is reproduced on Figure 1. The profiles slowly change with time and vary somewhat across the HMI CCDs.

2.1. Theoretical Algorithm

The MDI-like algorithm starts with a calculation of the first and second Fourier coefficients a_n and b_n of the Fe I line profile $I(\lambda)$ (λ is the wavelength):

$$a_1 = \frac{2}{T} \int_{-\frac{T}{2}}^{+\frac{T}{2}} I(\lambda) \cos\left(2\pi \frac{\lambda}{T}\right) d\lambda; \qquad b_1 = \frac{2}{T} \int_{-\frac{T}{2}}^{+\frac{T}{2}} I(\lambda) \sin\left(2\pi \frac{\lambda}{T}\right) d\lambda, \qquad (1)$$

$$a_2 = \frac{2}{T} \int_{-\frac{T}{2}}^{+\frac{T}{2}} I(\lambda) \cos\left(4\pi \frac{\lambda}{T}\right) d\lambda; \qquad b_2 = \frac{2}{T} \int_{-\frac{T}{2}}^{+\frac{T}{2}} I(\lambda) \sin\left(4\pi \frac{\lambda}{T}\right) d\lambda, \qquad (2)$$

where T is the "period" of the observation wavelength span, and nominally $T = 6 \times 68.8 = 412.8$ mÅ (*i.e.,* six times the nominal separation between two filters). MDI was designed so that the FWHM of its filter transmission profiles matches the FWHM of the Ni I line, and the four – equally spaced – wavelength samples cover a period equal to twice this FWHM. Consequently with MDI, and unlike HMI, nearly all of the spectral power in the solar line is captured by the first Fourier coefficients. HMI was not designed this way because the dynamic range corresponding to twice the FWHM of the Fe I line is too small to accommodate the large velocity variations resulting from the SDO orbit.

Assuming that the "pure" solar line, *i.e.* prior to its convolution by the HMI filter profiles, is a Gaussian:

$$I(\lambda) = I_c - I_d \exp\left[-\frac{(\lambda - \lambda_0)^2}{\sigma^2}\right], \qquad (3)$$

where I_c is the continuum intensity, I_d is the line depth, λ_0 is the Doppler shift, and σ is a measure of the line width (FWHM $= 2\sqrt{\log(2)}\sigma$), the Doppler velocity v can be expressed as

$$v = \frac{dv}{d\lambda} \frac{T}{2\pi} \text{atan}\left(\frac{b_1}{a_1}\right) \qquad (4)$$

with $dv/d\lambda = 299\,792\,458.0\,\mathrm{m\,s^{-1}}/6173.3433\,\text{Å} = 48\,562.4\,\mathrm{m\,s^{-1}\,\text{Å}^{-1}}$. The second Fourier coefficients could also be used:

$$v_2 = \frac{dv}{d\lambda}\frac{T}{4\pi}\,\mathrm{atan}\left(\frac{b_2}{a_2}\right). \tag{5}$$

The line depth $[I_d]$ is equal to

$$I_d = \frac{T}{2\sigma\sqrt{\pi}}\sqrt{a_1^2 + b_1^2}\,\exp\left(\frac{\pi^2\sigma^2}{T^2}\right) \tag{6}$$

while σ is equal to

$$\sigma = \frac{T}{\pi\sqrt{6}}\sqrt{\log\left(\frac{a_1^2 + b_1^2}{a_2^2 + b_2^2}\right)}. \tag{7}$$

HMI samples the iron line at six points and therefore only discrete approximations to the Fourier coefficients can be calculated, for instance:

$$a_1 \approx \frac{2}{6}\sum_{j=0}^{5} I_j \cos\left(2\pi\frac{2.5 - j}{6}\right). \tag{8}$$

The b_n are determined by a similar formula with cosine replaced by sine. These a_n and b_n are calculated separately for the LCP and RCP. Applying Equation (4) produces two velocities: v_{LCP} and v_{RCP}.

The "pure" Fe I line is not a Gaussian, and the discrete approximations to a_n and b_n are not accurate due to the reduced number of sampling points and because the filter profiles are not δ-functions (consequently the observables calculated are relative to the Fe I line convolved by the filters, not the "pure" line). Therefore, v_{LCP} and v_{RCP} must be corrected. Look-up tables obtained from a realistic model of the "pure" Fe I line at rest are used for this purpose. The line profile is shifted in wavelength to simulate a Doppler velocity. At each shift, the profile is convolved by the filter transmittances. The MDI-like algorithm is then applied to the simulated HMI intensities. The velocity returned by the algorithm is a function of the actual (input) Doppler velocity. The inverse function is called a look-up table (a misnomer that is a legacy of the MDI implementation). The tables vary across the HMI CCDs. They are linearly interpolated at v_{LCP} and v_{RCP} to derive corrected Doppler velocities V_{LCP} and V_{RCP}. In the rest of this article, first Fourier-coefficient MDI-like algorithm refers to the use of a_1 and b_1 to estimate the Doppler velocities and their subsequent correction with look-up tables.

Calibration of the HMI filters shows some residual errors (at the percent level) on their transmittances, resulting in imperfect look-up tables. Conversely, the SDO orbital velocity is known very accurately and can be used to partly improve these tables. This additional step is implemented in the HMI pipeline, but will be ignored here.

Finally, the V_{LCP} and V_{RCP} velocities are combined to produce a Doppler velocity estimate $[V]$:

$$V = \frac{V_{\mathrm{LCP}} + V_{\mathrm{RCP}}}{2} \tag{9}$$

while the LOS magnetic field strength $[B]$ is

$$B = (V_{\mathrm{LCP}} - V_{\mathrm{RCP}})K_m \tag{10}$$

where $K_m = 1.0/(2.0 \times 4.67\,10^{-5}\lambda_0 g_L c) = 0.231\,\mathrm{G\,m^{-1}\,s}$, $g_L = 2.5$ (Norton *et al.*, 2006) is the Landé g-factor, and c is the speed of light.

An estimate of the continuum intensity [I_c] is obtained by reconstructing the solar line from the Doppler shift, line-width, and line-depth estimates:

$$I_c \approx \frac{1}{6} \sum_{j=0}^{5} \left[I_j + I_d \exp\left(-\frac{(\lambda_j - \lambda_0)^2}{\sigma^2} \right) \right],   \tag{11}$$

where λ_0, I_d, and σ are the values retrieved by Equations (4), (6), and (7), and λ_j are the nominal wavelengths corresponding to each filter profile.

2.2. Actual Implementation

The algorithm is implemented slightly differently in the HMI pipeline. Tests on artificial Gaussian lines using the proper HMI filter transmittances showed that the theoretical algorithm overestimates the line width of "pure" Gaussian lines by $\approx 20\%$ for a line with $I_d = 0.62$ and $\sigma = 0.0613$ Å (values in Norton *et al.*, 2006). Conversely, the line depth is underestimated by $\approx 33\%$. The continuum intensity seems only slightly underestimated (by $\approx 1\%$). These errors on the parameters of artificial Gaussian lines arise because the number of wavelength samples is too small and the filters are not δ-functions.

Due to an initial error in implementation, a factor $K_1 = 5/6$ multiplies σ returned by Equation (7), while a factor $K_2 = 6/5$ multiplies I_d returned by Equation (6). The integral of a Gaussian is proportional to $I_d\sigma$; therefore, multiplying these two quantities by K_1 and $K_2 = 1/K_1$ keeps the integral constant and produces the same continuum intensity as Equation (11). In the current implementation, the line depths and line widths returned by Equations (6) and (7) are still intentionally multiplied by K_2 and K_1, respectively, so that both values are expected to be closer to the actual ones, while the continuum intensity remains unchanged. In this article, we only consider line widths and line depths corrected by K_1 and K_2 when referring to the MDI-like algorithm.

Finally, when computing line depth and continuum intensity with Equations (6) and (11), the σ used in these equations is not the one derived from Equation (7), which is saved in the observables series. A fifth-order polynomial was fitted to an azimuthal average (about the solar disk center) of an HMI line-width map obtained from Equation (7) (and corrected by K_1) during a period of low solar activity, as a function of center-to-limb distance. Line widths calculated from this polynomial are used instead of those from Equation (7), because the latter sometimes returns spurious values in the presence of locally strong magnetic fields, especially for pixels away from solar disk center.

3. Other Observables Algorithms Tested

Algorithms other than the MDI-like one based on a_1 and b_1 are also applied to IBIS data: an MDI-like algorithm with the second Fourier coefficients, a least-squares fit with a Gaussian profile for the Fe I line, and a least-squares fit with a Voigt profile.

Before the launch of SDO we considered averaging the results of both the first and second Fourier coefficients when computing Doppler velocity and field strength, and later transitioning to a least-squares fit. The second Fourier coefficients have half the dynamic range of a_1 and b_1, but the latter are used to properly offset the velocity v_2 (returned by a_2 and b_2) by the required amount when v (returned by a_1 and b_1) is outside the dynamic range of a_2 and b_2. Using the second Fourier coefficients turned out to be more difficult than anticipated: there were a significant number of saturated pixels where the magnetic field is strong, and

the velocities calculated differed significantly from the first Fourier-coefficient ones. Due to tight time constraints, we postponed the implementation of the second Fourier-coefficients algorithm. Therefore, only half the information available is utilized and the rms variation on Doppler velocity due to photon noise is larger. A possible improvement to the HMI pipeline would be to include these second Fourier coefficients; the impact is discussed here.

The MDI-like algorithm is computationally very fast: no fit is involved, only a combination of six wavelengths followed by a linear interpolation. That is one reason why this algorithm is currently preferred over least-squares fits. However, the look-up tables are computed for a reference Fe I profile in the quiet Sun; therefore, the algorithm is expected to fare poorly in regions of strong magnetic fields. Conversely, a least-squares fit with a reasonable model of the Fe I line should provide more accurate results, because the profile is adjusted in depth and width during the fit to reflect the presence of magnetic fields. The simplest model of the Fe I line used here is a Gaussian, resulting from Doppler broadening alone. It is a poor approximation to the iron line. A more elaborate model is the Voigt profile: a convolution between a Gaussian profile (thermal broadening) and a Lorentzian profile (produced by radiative and collisional broadenings). It is more representative of the actual Fe I line, even though it is symmetrical around the central wavelength, while the solar line displays a significant asymmetry. The Voigt profile implemented is characterized by five quantities: a Doppler shift [λ_0], a line width [σ] of the Gaussian part of the profile, a continuum intensity [I_c], a scale parameter [I_d] related to the line depth, and a damping parameter [a]. Least-squares fits of three observed Fe I line profiles, provided by R. Ulrich (private communication, 2011) at different solar center-to-limb distances and obtained at Mount Wilson Observatory, return values for a in the range $0.16 - 0.2$, while fits on Kitt Peak atlas data return $a = 0.25$. This is close to the $a = 0.23$ quoted by Bell and Meltzer (1959). Here we set $a = 0.225$, but the exact value has little impact on the conclusions of this article (we tested lower values).

4. IBIS Data

Rajaguru *et al.* (2010) detail the IBIS data and Milne–Eddington (M–E) inversion utilized here. The first hour of observation is selected, corresponding to the best seeing interval. The initial datacube format is $512 \times 512 \times 23 \times 4 \times 79$, where the first two dimensions refer to the Cartesian coordinates on the CCD (the original 1024×1024 IBIS data were rebinned by a factor two), the next dimensions are the number of wavelength samples (23) and of Stokes parameters (4), and the last dimension is the number of time steps (the datacube spans 1.03 hours at a cadence of 47.5 seconds). To compare the LOS magnetic-field strength returned by the observables algorithms with the result of the M–E inversion of the Stokes vector, we follow Rajaguru *et al.* (2010) and select a 341×341 pixel region centered on the sunspot. The M–E inversion in Rajaguru *et al.* (2010) was performed on a one-hour temporal average of the data to reduce the noise level; therefore, we also average the datacube over one hour, despite the smoothing of the line profiles that such averaging produces. We only consider the LCP ($I + V$) and RCP ($I - V$) polarizations. The final datacube contains $341 \times 341 \times 23 \times 2$ points. At each pixel, a cubic-spline interpolation is applied (a quadratic interpolation was also tested) of the 23 wavelength samples, to obtain LCP and RCP profiles on a finer wavelength grid with a sampling rate of 0.5 mÅ.

Figure 2 shows maps of the LOS observables for the temporally averaged IBIS data, obtained with the first Fourier-coefficients MDI-like algorithm. The square window centered on the sunspot shows the area selected for various plots of Section 5. Outside this window
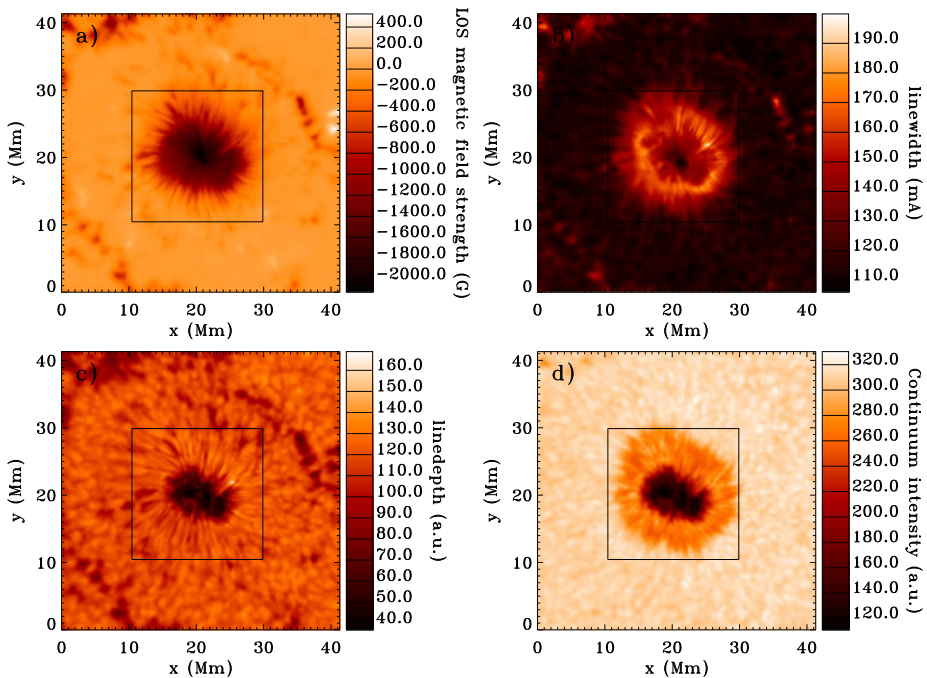
Figure 2 Situation maps showing the LOS observables obtained with the first-Fourier coefficient MDI-like algorithm. (a) Magnetic field strength (the color scale is truncated); (b) line width; (c) line depth; (d) continuum intensity. The active region NOAA AR 10960 was observed by the IBIS instrument on 8 June 2007. The square window centered on the sunspot shows the pixels selected for various figures of Section 5.

the M–E inversion is very noisy due to the low polarization signal. No attempt was made to correct for scattered light on IBIS observations; therefore, the signal in the sunspot umbra partly comes from adjacent areas and especially from the penumbra. The M–E inversion was performed on the raw IBIS line profiles; *i.e.,* no deconvolution by the IBIS filter profiles was attempted because the profiles were not available at the time that the inversion was made. A deconvolution of a typical IBIS Stokes-*I* profile by a Gaussian with FWHM = 25 mÅ produces a deconvolved line close to the original one (the FWHM is reduced by only $\approx 2.5\%$, while the line depth is increased by a similar amount). Therefore, using spectrally convolved lines instead of deconvolved ones should have little impact on the conclusions of this article.
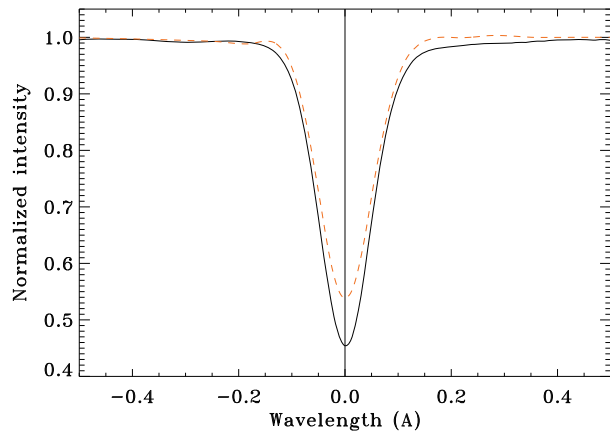
5. Results

To simulate the 12 HMI filtergrams needed to derive LOS observables, a set of HMI filter-transmission profiles obtained from calibration procedures and valid at solar disk center is used. The temporally averaged wavelength-interpolated LCP and RCP IBIS profiles are convolved by the filter profiles, resulting in simulated HMI intensities.

The look-up tables required by MDI-like algorithms necessitate a reference Fe I line, usually taken at rest. Therefore, a Stokes-*I* profile is selected, for which the $I + V$ and $I - V$ components superimpose (denoting the absence of any significant magnetic field).

Figure 3 Comparison of Fe I
line profiles: the black solid line
is from the Kitt Peak atlas
obtained with the Kitt Peak
McMath–Pierce telescope, while
the dashed orange line is the
reference profile used here to
calculate look-up tables for the
MDI-like algorithms and
obtained from an hour-long
average of IBIS data in a
quiet-Sun pixel.

The resulting line is shown on Figure 3. The magnetic-field strength is negligible at several locations in the IBIS field of view, and several reference profiles were tested; despite minor differences, our conclusions are unaffected by a specific choice. The reference profile selected is broader (with an FWHM of 116.8 mÅ instead of 102 mÅ) and shallower (with a line depth of 0.461 instead of 0.66) than the line parameters reported by Norton *et al.* (2006). The difference mainly comes from the temporal averaging of IBIS data, the difference in spatial resolution, and to a lesser extent from the convolution of the IBIS line by the instrumental transmittance and the presence of instrumental scattered light.

5.1. Doppler Velocity and LOS Magnetic Field Strength

Figure 4 displays the Doppler velocity and LOS magnetic field strength returned by the different observables algorithms. It is a cut at the latitude crossing the center of the sunspot. The average velocity returned by each algorithm in a nearby quiet-Sun region has been subtracted to facilitate comparisons. The curves labeled "line core" show the velocity and field strength obtained by locating the minimum of the interpolated Fe I profiles: once the approximate location is known, a second-order polynomial fit is performed in the wavelength range $[-25, +25]$ mÅ around this location, to determine the exact minimum location. Line-core velocities are not expected to match other algorithms' velocities; *e.g.*, Fleck, Couvidat, and Strauss (2011) showed that the MDI-like algorithm based on a_1 and b_1 does not track the Doppler shift of the core of the line but rather of its center of gravity, as expected. Other algorithms are sensitive to different parts of the Fe I line, corresponding to different atmospheric heights. In the sunspot, the MDI-like algorithm with a_1 and b_1 returns velocities that are larger than the least-squares-fits values, by up to 300 m s^{-1}, with an average difference of about 90 m s^{-1} in the umbra. In the quiet Sun all of the velocities are similar (due to the subtraction of the respective averages). Table 1 lists the linear (Pearson) correlation coefficients between velocities returned by different algorithms. The lowest correlation is obtained between the second Fourier-coefficients MDI-like algorithm and line-core velocities.

In the sunspot, the second Fourier-coefficient MDI-like algorithm behaves differently than the other algorithms, sometimes returning large negative velocities where the others return positive ones (*e.g.* at $x = 15$ Mm on the upper panel of Figure 4, the second Fourier coefficients return $v_2 \approx -400$ m s^{-1} while the first Fourier coefficients return $v \approx +150$ m s^{-1}), and *vice versa*. In the penumbra especially, the second Fourier-coefficients velocities are strikingly different from those returned by the first-Fourier coef-
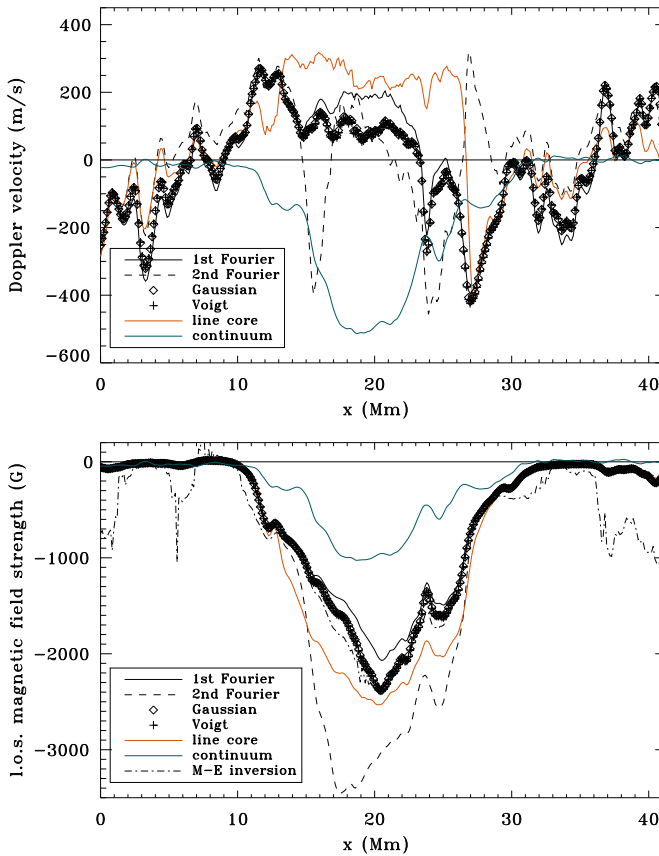
Figure 4 Doppler velocities (upper panel) and LOS magnetic-field strengths (lower panel) returned by various observables algorithms. This is a cut at the latitude crossing the center of the sunspot. The curve labeled "continuum" shows a normalized continuum intensity for comparison. On the upper panel, the average velocity in the quiet Sun returned by each algorithm has been subtracted.

Table 1 Pearson linear correlation coefficients between Doppler velocities returned by different algorithms for the pixels located in the square window of Figure 2.

	1st Fourier	2nd Fourier	Gauss	Voigt	Line core
1st Fourier	100.0	35.0	99.4	99.3	79.5
2nd Fourier	35.0	100.0	37.8	37.8	24.6
Gauss	99.4	37.8	100.0	99.9	77.6
Voigt	99.3	37.8	99.9	100.0	77.5
Line core	79.5	24.6	77.6	77.5	100.0

ficients and the least-squares fits. Figure 5 shows the velocity maps obtained with the two MDI-like algorithms, confirming the discrepancy.

The algorithms' ability to retrieve a correct velocity was tested by simulating Doppler shifts: LCP Fe I line profiles were selected at three different pixel locations (in the quiet Sun,

Table 2 Standard deviation [m s^{-1}] of Doppler velocity retrieved by the LOS algorithms and resulting from photon noise, for three different Doppler velocities.

Velocity [m s^{-1}]	1st Fourier	2nd Fourier	Gauss	Voigt
−2016	19.18	32.48	15.66	15.76
0	19.17	29.24	14.96	14.80
+2016	19.35	30.45	15.80	15.98

Table 3 Pearson linear-correlation coefficients between LOS magnetic field strengths returned by different algorithms for the pixels located in the square window of Figure 2.

	1st Fourier	2nd Fourier	Gauss	Voigt	M–E LOS field
1st Fourier	100.0	96.4	99.8	99.8	95.3
2nd Fourier	96.4	100.0	97.0	97.0	94.8
Gauss	99.8	97.0	100.0	99.9	95.8
Voigt	99.8	97.0	99.9	100.0	95.8
M–E LOS field	95.3	94.8	95.8	95.8	100.0

in the penumbra, and in the umbra; see Figure 6), and were shifted in wavelength to simulate the impact of a Doppler velocity. The observables algorithms were then applied to the intensities derived from these shifted lines. The result is shown on Figure 7 (notice the different scale on the upper panel). In the quiet Sun and in the velocity range [−5, +5] km s^{-1}, the four algorithms behave similarly and the difference between the retrieved velocity and the actual one (*i.e.* the error on velocity) does not vary much (the second Fourier-coefficients algorithm displays the largest variation, ≈ 75 m s^{-1}). The offsets between the curves may reflect the difference in sensitivity to various parts of the Fe I line. The initial guess for the least-squares fits is provided by the first Fourier-coefficients MDI-like algorithm; if a zero velocity is used instead, the fits do not converge for velocities larger than ≈ 3.5 km s^{-1} (in absolute value). In the penumbra and umbra, the first Fourier-coefficients algorithm and the least-squares fits behave similarly in the velocity range ≈ [−5, +5] km s^{-1}. The second Fourier-coefficients algorithm behaves differently and shows a larger dependence on input velocity. Moreover, the velocity error is significantly different in the umbra and penumbra. The second Fourier-coefficients algorithm fares poorly compared to the other algorithms.

The standard deviation of Doppler velocity resulting from photon noise was computed in the quiet-Sun pixel for the different LOS algorithms, assuming an exposure time long enough to fill the HMI CCD well (*i.e.* an exposure level of 175 000 photons): the results are listed in Table 2. The standard deviations of the least-squares fits are smaller than those of the MDI-like algorithms. The second Fourier-coefficients algorithm has the largest standard deviation. Noticeably, an unweighted average of the velocities returned by the two MDI-like algorithms will only lower the standard deviation by less than 10% (and not $\sqrt{2}$ as might have been expected) compared to the first Fourier coefficients alone.

Table 3 lists the correlation coefficients between LOS magnetic-field strengths. In this table and in the rest of the paper, M–E LOS field refers to the field strength inverted by the Milne–Eddington code and multiplied by the cosine of the field-inclination angle [Φ] (relative to the vertical direction). The lowest correlation is obtained between the second Fourier-coefficients MDI-like algorithm and M–E inversion. In the sunspot umbra, the LOS
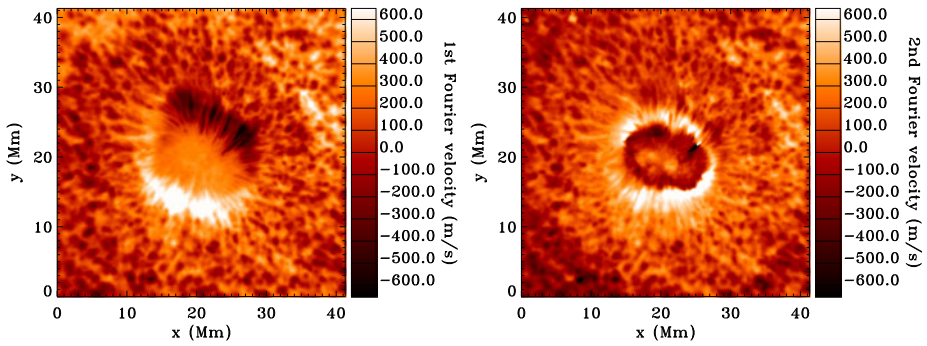
Figure 5 Doppler velocities returned by the MDI-like algorithm using the first (left panel) or second (right panel) Fourier coefficients.

Figure 6 Comparison of Fe I line profiles from temporally averaged wavelength-interpolated IBIS data: the solid line is from a quiet-Sun pixel, the dashed red line is from a penumbral pixel, and the dash-dotted green line is from an umbral pixel. The profiles are normalized by their respective continuum intensities.
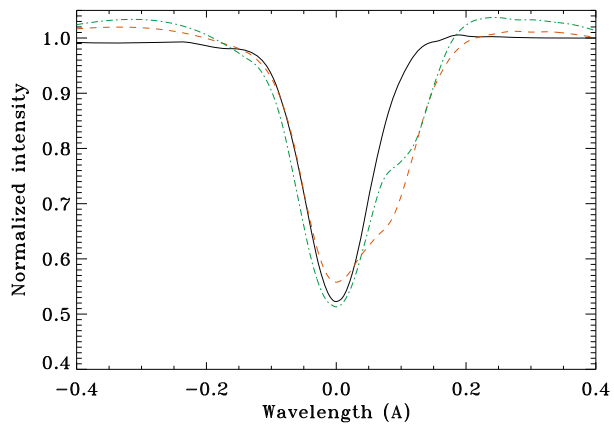
magnetic-field strength returned by a_2 and b_2 is very different from the other algorithms (see Figure 4).

Even though we compare field strengths returned by various algorithms to the M–E inversion (used as a reference), remember that the Milne–Eddington atmosphere model is only approximate. In particular, the atmospheric parameters are assumed to be height-independent, which is contradicted by the C-shape of the Fe I line bisector. The magnetic-field inclination angle and strength also vary with height. Therefore, the observables algorithms are not expected to match the M–E results or to each return the same LOS field strengths, because of their different atmospheric-height sensitivities.

Figure 8 shows the impact of the M–E field inclination angle [Φ] on the relative error in LOS field strength made by each algorithm. This relative error is the strength returned by an algorithm minus the M–E LOS field strength, divided by the M–E strength. For the first Fourier-coefficients MDI-like algorithm and least-squares fits, this error first decreases (in absolute value) when the inclination angle increases from 0 to ≈ 35 degrees (corresponding to the sunspot umbra), is relatively stable and small for Φ in the range $\approx 35 - 60$ degrees (corresponding to the inner penumbra), and then increases steeply for $\Phi \gtrsim 65$ degrees (outer penumbra). On this plot, only the pixels with an absolute field strength > 150 G and located inside the square window of Figure 2 are shown, thus avoiding the noisiest values. The error on the M–E inverted field strength and the error on Φ both increase with Φ, which could
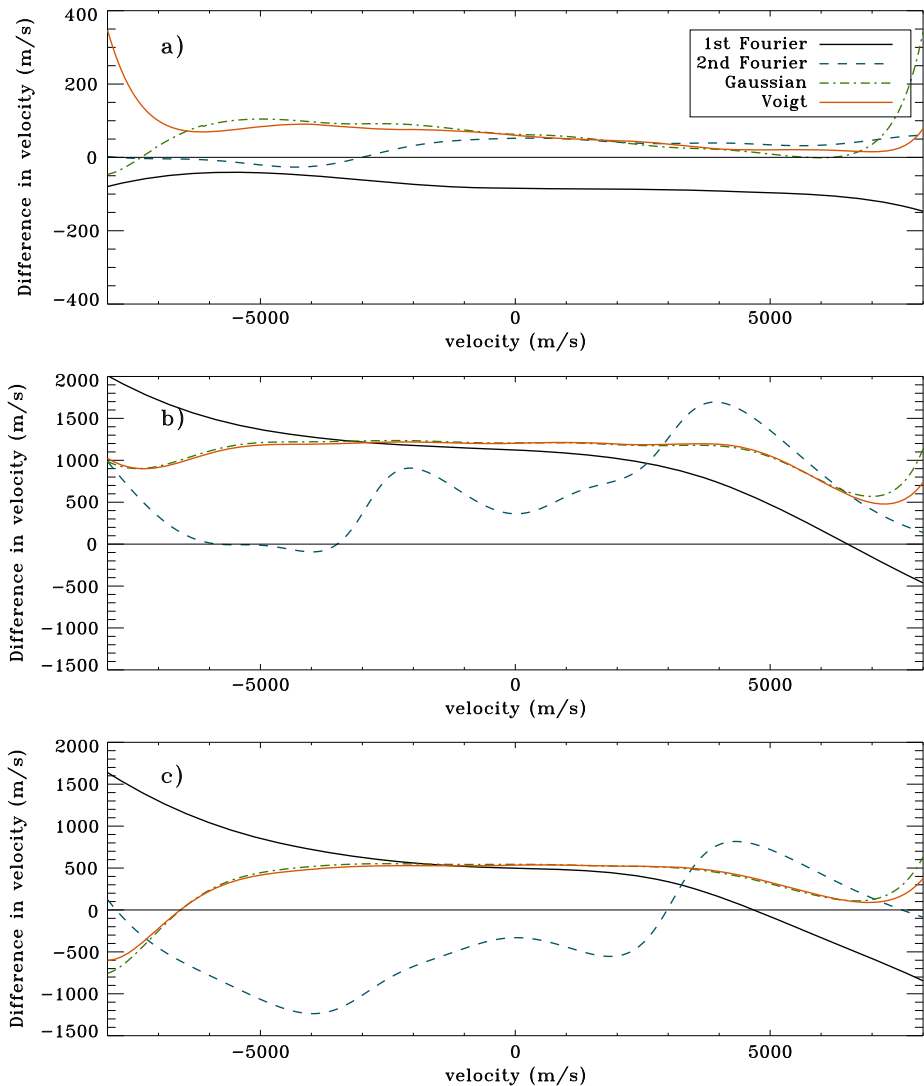
Figure 7 Difference in Doppler velocity retrieved by different algorithms and the input velocity v_{in}, as a function of v_{in}. Solid line: first Fourier-coefficients MDI-like algorithm; dashed blue line: second Fourier-coefficients MDI-like algorithm; dash-dotted green line: least-squares fit with a Gaussian profile; dash-triple–dotted orange line: least-squares fit with a Voigt profile. (a) is for a quiet-Sun pixel, (b) for a penumbral pixel, and (c) for an umbral pixel. The scale on the upper panel differs from that of the other panels.

explain the larger relative error on the field strength for $\Phi \gtrsim 65$ degrees. Overall, this relative error seems lower (in absolute value) in the sunspot penumbra than in the umbra.

None of the observables algorithms show any dependence on the azimuth angle of the magnetic field.

Figure 9 shows the impact of Φ on the difference in Doppler velocity with the line-core velocity. The absolute value of this difference does not matter much as different algorithms are sensitive to different heights in the solar atmosphere – what matters is the dependence of
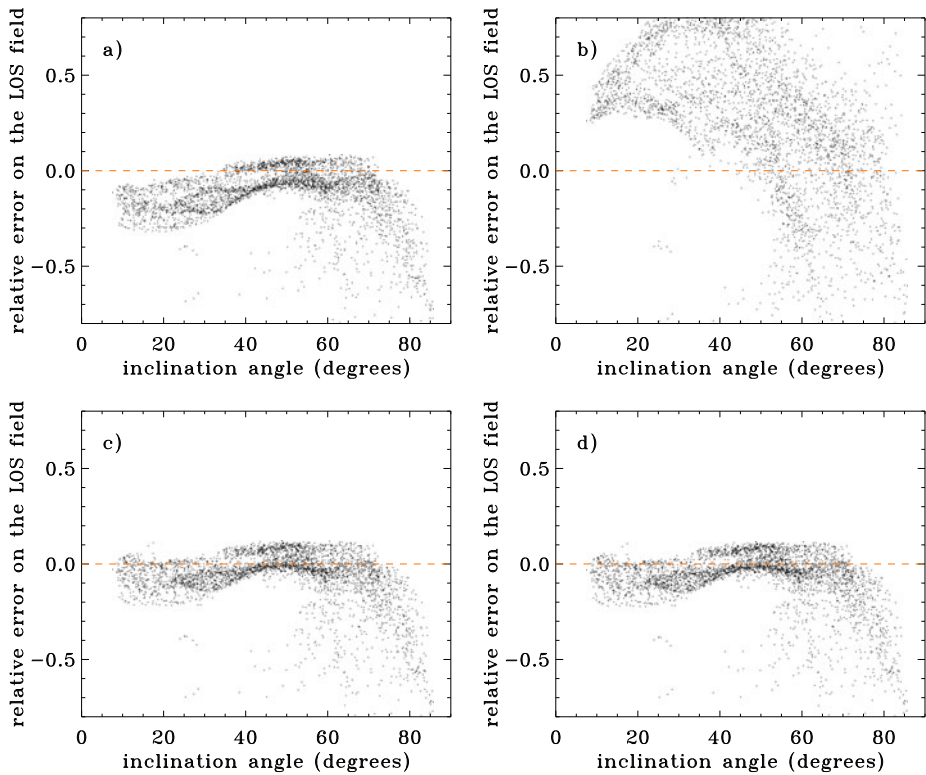
Figure 8 Ratio of the difference between LOS magnetic field strength returned by the observables algorithms and M–E LOS field strength to the M–E LOS field strength, as a function of the field inclination angle [Φ]. (a) MDI-like algorithm with first Fourier coefficients; (b) MDI-like algorithm with second Fourier coefficients; (c) least-squares fit with a Voigt profile; (d) least-squares fit with a Gaussian profile. Only the pixels with an absolute field strength > 150 G and located inside the square window of Figure 2 are shown.

this difference on the inclination angle. The first Fourier-coefficients MDI-like algorithm and the least-squares fits behave in a similar fashion: the difference in velocity slightly increases, in absolute value, with Φ in the range ≈ 0 – 60 degrees, and then it changes steeply. The MDI-like algorithm with second Fourier coefficients behaves differently and shows a larger dispersion in velocity difference. In absolute value, these differences are larger in the sunspot inner penumbra than in the umbra.

On Figure 10, the fields weaker (in absolute value) than 1250 G (black dots) are isolated from stronger fields (orange dots). The Doppler-velocity scatter plots show almost separate orange and black branches: the relation between the velocities returned by the four algorithms and the line core velocities depends on the field strength. Different field strengths may correspond to different parts of the sunspot. As previously observed, the first Fourier-coefficients MDI-like, Gaussian least-squares, and Voigt least-squares algorithms behave similarly, unlike the second Fourier-coefficients algorithm which returns spurious velocities in regions of strong fields. Indeed, the orange branch of the upper-right panel of Figure 10 is nearly vertical, and differs greatly from the black branch. Figure 11 shows scatter plots of the LOS field strength, and the lower-right panel highlights the similarity of the values returned by the two least-squares fits.
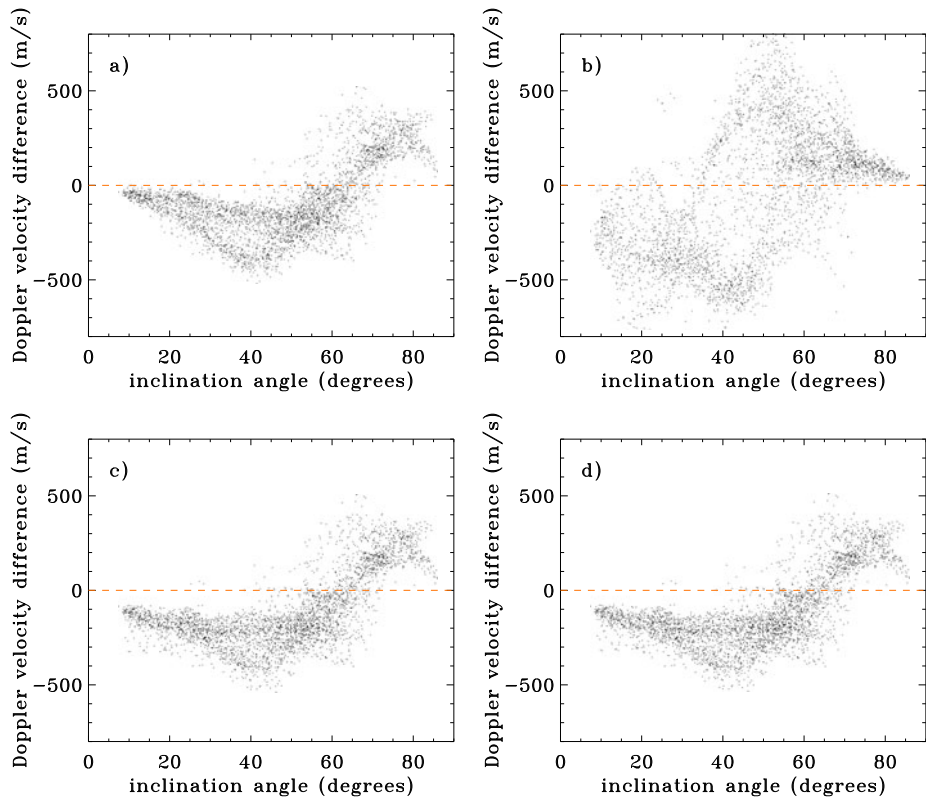
Figure 9 Differences in Doppler velocity returned by the observables algorithms with line-core velocity, as a function of the field-inclination angle [Φ]. (a) MDI-like algorithm with first Fourier coefficients; (b) MDI-like algorithm with second Fourier coefficients; (c) least-squares fit with a Voigt profile; (d) least-squares fit with a Gaussian profile. Only the pixels with an absolute field strength > 150 G and located inside the square window of Figure 2 are shown.

Although the previous results have been presented as if the impacts of field strength and inclination angle were separable, these two quantities are related in a sunspot: strong fields – mostly located in the umbra and stronger than 1600 G in absolute value – have small inclinations ($\Phi \lessapprox 35$ degrees), while weaker fields – mostly in the penumbra – have large inclinations. Another consideration affecting the results is that the geometric height in the atmosphere where the Doppler signal is formed is not the same above the quiet Sun and above a sunspot.

Overall, least-squares fits perform better than the first Fourier-coefficients MDI-like algorithm in the presence of a magnetic field, while the second Fourier-coefficients algorithm appears to be the least accurate algorithm. a_2 and b_2 are very sensitive to the Fe I line shape, much more so than a_1 and b_1. The deformation affecting the $I + V$ and $I - V$ components in the presence of a strong and inclined field (see the $I + V$ components on Figure 6) is not reflected in the look-up tables obtained from a line at rest. This explains the difficulties encountered during the commissioning phase of SDO when trying to use a_2 and b_2. The other algorithms tested are more robust in the presence of a field.

Averaging Doppler velocities and magnetic-field strengths obtained from the first and second Fourier coefficients might not be beneficial to these observables: in the quiet Sun it
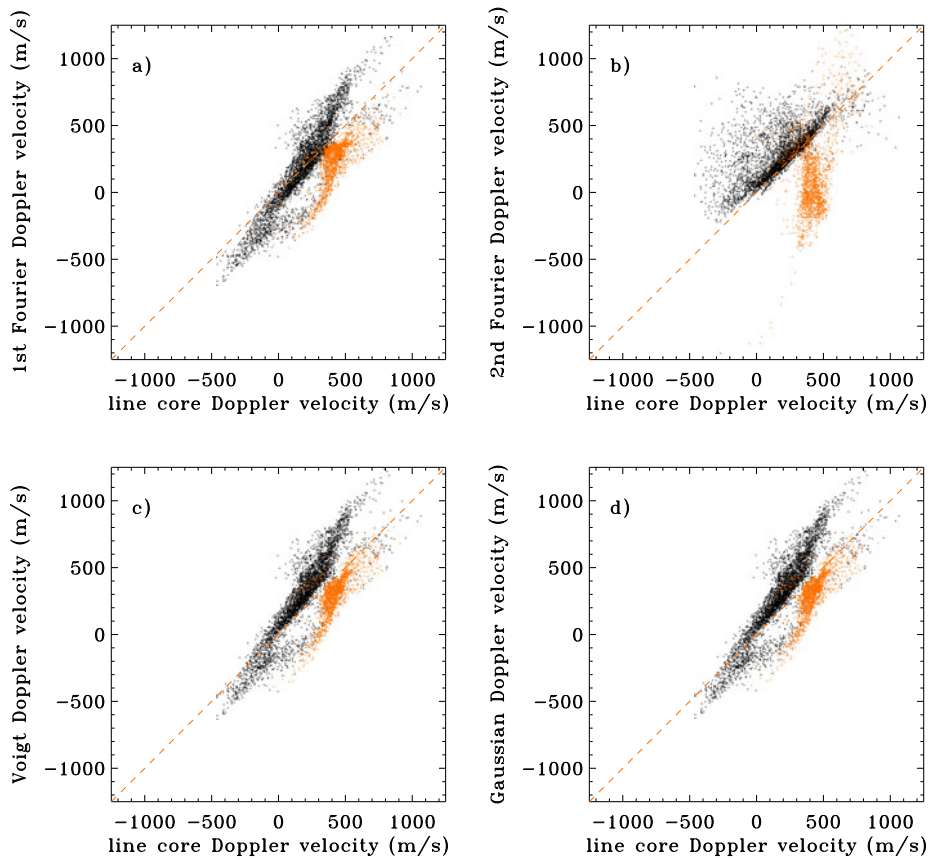
Figure 10 Scatter plots of the Doppler velocities returned by different algorithms with the line-core velocity. (a) First Fourier-coefficient MDI-like algorithm; (b) second Fourier-coefficient MDI-like algorithm; (c) least-squares fit with a Voigt profile; (d) least-squares fit with a Gaussian profile. Black dots: absolute magnetic field strength < 1250 G; orange dots: absolute magnetic-field strength > 1250 G.

will reduce the noise level due to photon noise (although by a factor smaller than $\sqrt{2}$) and it may improve the accuracy of the results, but it is likely to degrade it in the presence of strong magnetic fields.

Measurements based on the data of Figure 8 show that the first Fourier-coefficient MDI-like algorithm underestimates (in absolute value) the LOS field strength in a sunspot umbra (here defined as $\Phi < 35$ degrees) by an average value of $\approx 17\%$. Conversely, the second Fourier-coefficients MDI-like algorithm overestimates this field strength, by more than 50% for many pixels. The least-squares fit (with a Gaussian or Voigt profile) provides more accurate results, but still underestimates the actual LOS field strength in the umbra (by $7-8\%$ on average). The Voigt profile does not seem to improve the determination of the LOS observables compared to the simpler Gaussian one. The implementation of the Voigt profile makes line depth and line width slightly more difficult to determine than with a basic Gaussian, because these quantities must be calculated from the fitted quantities I_d and σ (with a relation depending on the damping parameter a).
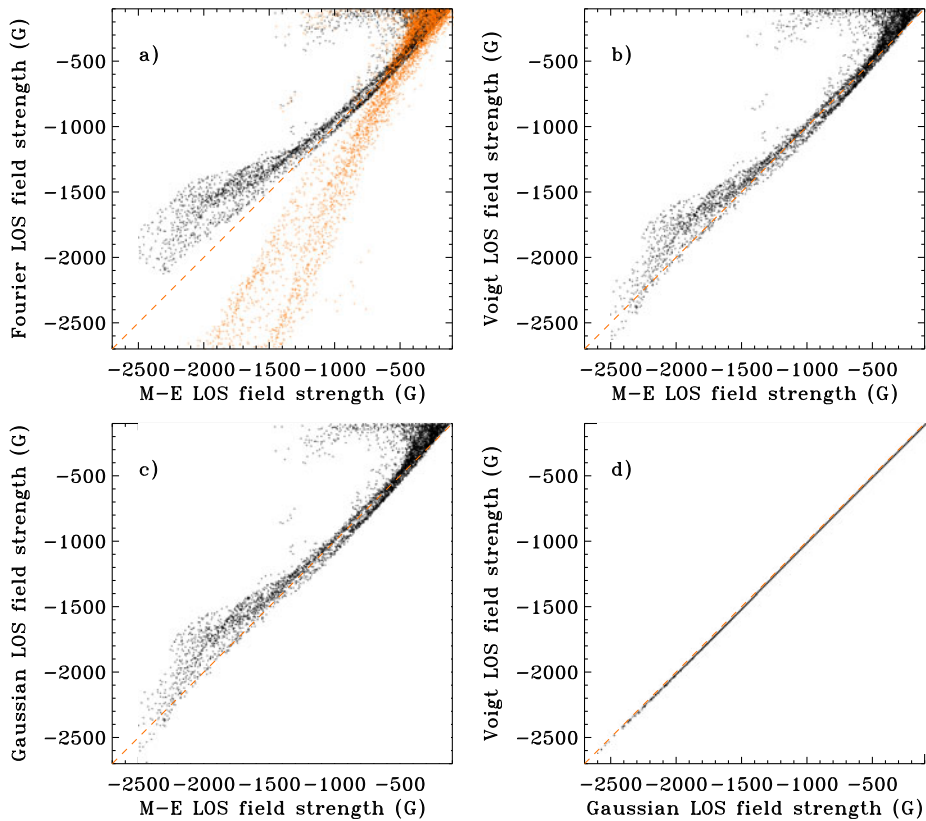
Figure 11 Scatter plots of LOS magnetic-field strengths returned by different algorithms with LOS field strength returned by the M–E inversion. (a) First (in black) and second (in orange) Fourier-coefficients MDI–like algorithms; (b) least-squares fit with a Voigt profile; (c) least-squares fit with a Gaussian profile; (d) scatter between least-squares fits with Voigt and Gaussian profiles.

## 5.2. Other Observables Quantities: Line Width, Line Depth, and Continuum Intensity

With IBIS data, the line width, line depth, and continuum intensity returned by the observables algorithms can be compared to those quantities measured from the wavelength-interpolated line profiles (with a fine enough wavelength grid). The measured continuum intensity is the intensity of the Fe I profile at a wavelength [λ] far enough from line center (we selected $\lambda = -0.63$ Å). Figure 12 is a collection of scatter plots of the line width returned by different algorithms, Figure 13 shows the line depth, and Figure 14 shows the continuum intensity. On these three figures, the pixels with M–E inclination angle $\Phi < 35°$ (roughly corresponding to the umbra) are separated from those with a more inclined field on the left panels, and the pixels with a field weaker than 1250 G (in absolute value) are separated from those with a stronger field on the right panels. The measured quantities are directly obtained from the interpolated IBIS profiles: the LCP and RCP components are processed separately and their values averaged. For the algorithms tested, the dispersion of the line width relative error (see Figure 15) increases with the magnetic-field strength and for less inclined fields: the line widths returned are less robust in the sunspot umbra than in the penumbra and the quiet Sun. Line-depth (see Figure 16) and continuum-intensity relative
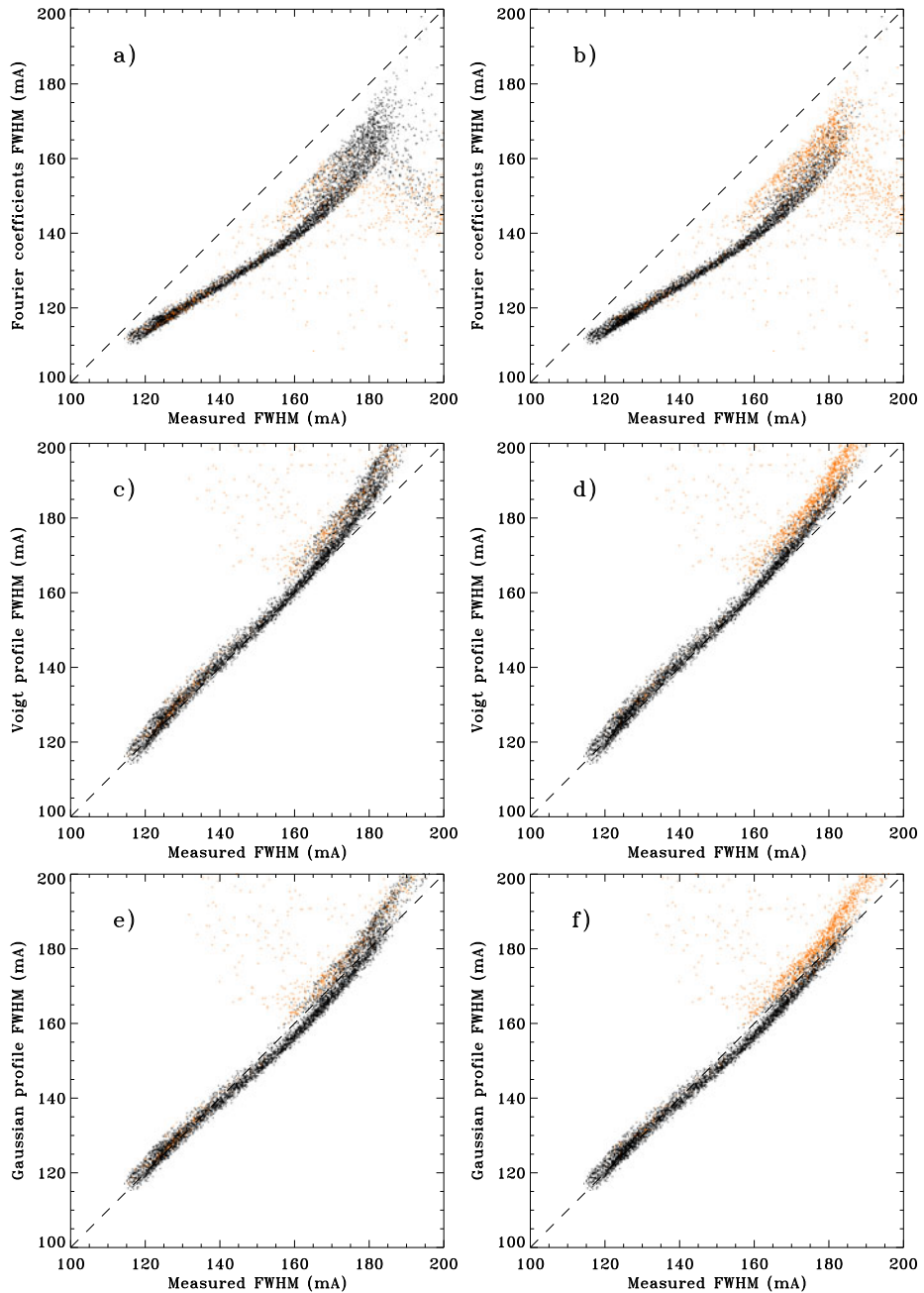
Figure 12 Scatter plots of FWHMs returned by different algorithms with actual (measured) FWHMs. (a) and (b) MDI-like algorithm; (c) and (d) least-squares fit with a Voigt profile; (e) and (f) least-squares fit with a Gaussian profile; (a), (c), and (e) the black dots show pixels for which the magnetic-field inclination is larger than 35°, while the orange dots are for less inclined fields; (b), (d), and (f) the black dots show pixels for which the absolute magnetic-field strength is < 1250 G, while the orange dots are for stronger fields.
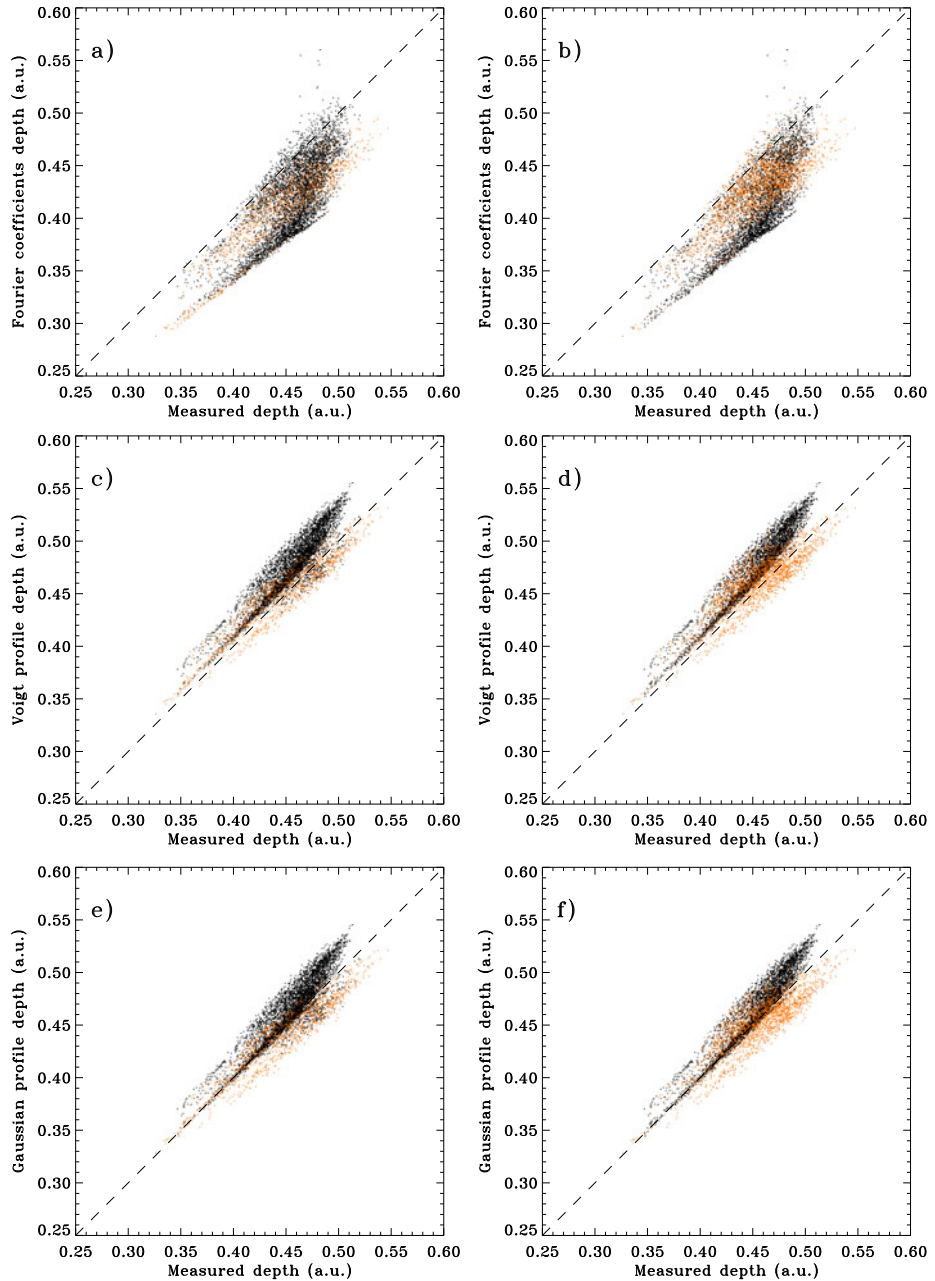
Figure 13 Scatter plots of line depths returned by different algorithms with actual (measured) line depths. (a) and (b) MDI-like algorithm; (c) and (d) least-squares fit with a Voigt profile; (e) and (f) least-squares fit with a Gaussian profile. (a), (c), and (e) the black dots show pixels for which the magnetic-field inclination is larger than 35°, while the orange dots are for less inclined fields; (b), (d), and (f) the black dots show pixels for which the absolute magnetic-field strength is < 1250 G, while the orange dots are for stronger fields.
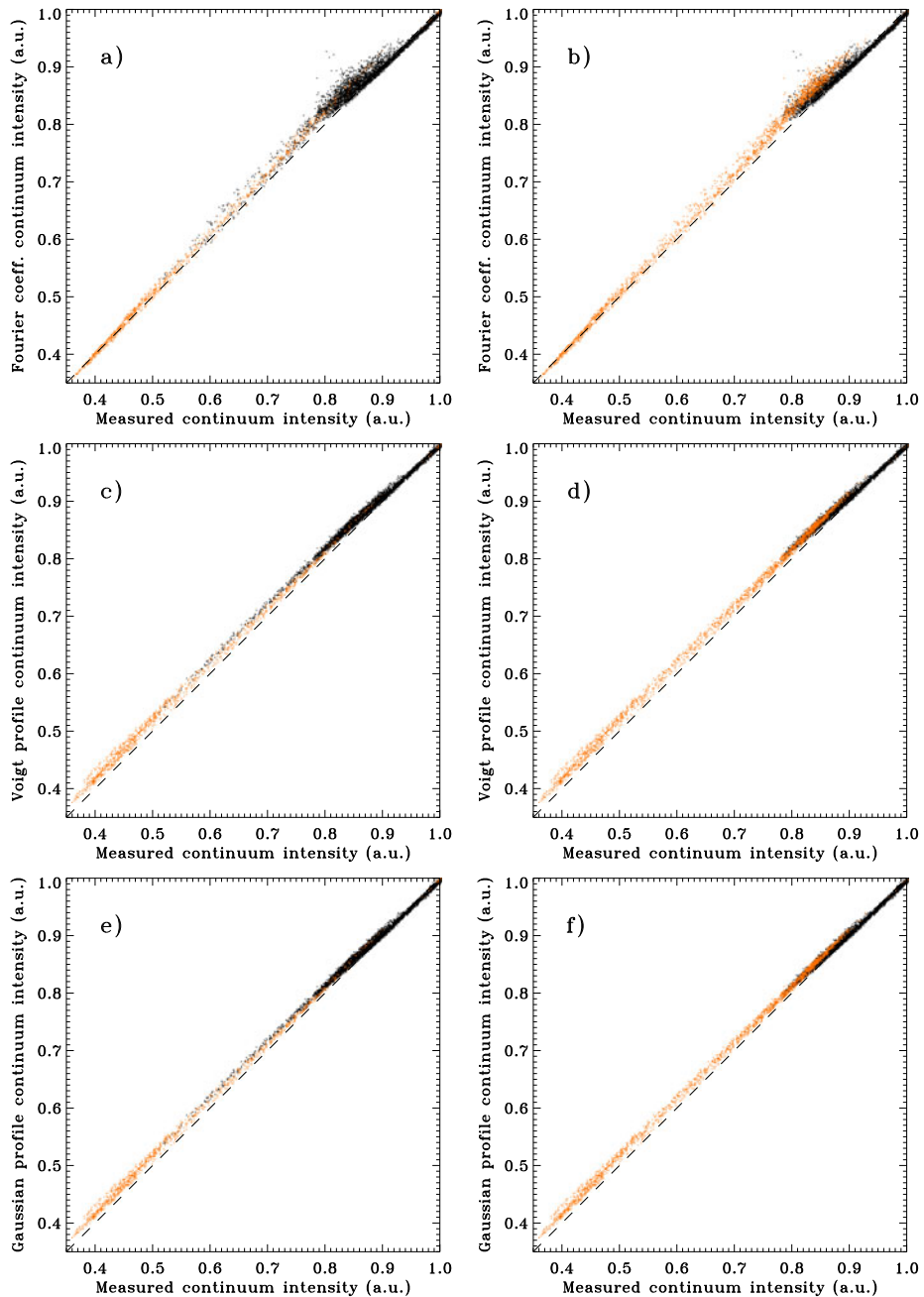
Figure 14 Scatter plots of (normalized) continuum intensities returned by different algorithms with actual (measured) continuum intensities. (a) and (b) MDI-like algorithm; (c) and (d) least-squares fit with a Voigt profile; (e) and (f) least-squares fit with a Gaussian profile. (a), (c), and (e) the black dots show pixels for which the magnetic-field inclination is larger than 35°, while the orange dots are for less inclined fields; (b), (d), and (f) the black dots show pixels for which the absolute magnetic-field strength is < 1250 G, while orange dots are for stronger fields.

errors also show an increase in dispersion with field strength. The average relative errors on the line width are larger for strong fields (here we considered fields > 1600 G in absolute value). Again, the MDI-like algorithm (using both first and second Fourier coefficients for these quantities) fares relatively poorly in the presence of a magnetic field, significantly underestimating the line width in the sunspot umbra and penumbra (by an average of ≈ 17.5% for strengths > 1600 G in absolute value). As already mentioned, a strong and inclined field distorts the Fe I line. With Zeeman splitting, the σ components of a longitudinal field are contaminated by the π component when Φ is different from 0; the resulting profiles are different from the Gaussian assumed when deriving Equations (6) and (7). The MDI-like algorithm also underestimates, by an average of ≈ 3.9%, the actual line width in the quiet Sun; even in the absence of a field the Fe I line is not a Gaussian and is asymmetrical. Therefore, the factor K_1 could be revised upward. Least-squares fits provide more robust line-width and line-depth values (smaller dispersion in their relative errors). Surprisingly, for the MDI-like algorithm the average relative error on line depth seems lower for stronger magnetic fields than for weaker ones. If only quiet Sun pixels are selected (*e.g.* fields weaker than 50 G in absolute value), the MDI-like algorithm underestimates the actual line depth by ≈ 16% (see Figure 16). This occurs after I_d returned by Equation (6) has been multiplied by K_2; this factor could also be revised upward. For stronger fields (> 1000 G in absolute value), the relative error on line depth returned by the MDI-like algorithm is smaller (≤ 11.5% on average), and for a few pixels is even zero. In contrast, for the least-squares fits the relative error on line depth runs both ways in the presence of stronger fields and is ≤ 3.8% on average in absolute value. In the quiet Sun, the least-squares fits overestimate the line depth by < 2.8% on average.

The continuum intensity obtained from the MDI-like algorithm is slightly underestimated by ≈ 1.7% on average in the quiet Sun, while the least-squares fit with a Voigt profile overestimates the intensity in the quiet Sun by ≈ 0.7%, and the least-squares fit with a Gaussian underestimates it by 0.15% on average. On Figure 14, for the MDI-like algorithm the slopes of the curves are different for stronger and weaker fields and for smaller and larger inclination angles. This effect seems absent with the least-squares fits.

6. Conclusion

Spectropolarimetric images of the solar surface obtained by the IBIS instrument were used to investigate the accuracy of LOS observables returned by the MDI-like algorithm implemented in the processing pipeline of the SDO/HMI instrument. Three other observables algorithms were also tested: an MDI-like algorithm based on the second Fourier coefficients, a least-squares fit with a Gaussian profile, and a least-squares fit with a Voigt profile. In the presence of magnetic fields, the least-squares fits are more accurate than the MDI-like algorithms (as expected). The second Fourier-coefficient MDI-like algorithm fares especially poorly in a sunspot, probably due to the significant distortion of the $I + V$ and $I - V$ Stokes profiles in strong and inclined magnetic fields compared to the line at rest. In a contrived way, one could improve the MDI-like algorithm by implementing different look-up tables, depending on the variation of a reference Fe I line model with magnetic-field strength and inclination, and using these tables in the presence of a magnetic field. Alternatively, a weighting scheme could be used to combine first and second Fourier-coefficients results, and to reduce the impact of second Fourier coefficients in strong fields. Combining first and second Fourier-coefficients results for Doppler velocity and LOS field strength is appealing in the quiet Sun to reduce the noise level due to photon noise (although by a factor smaller
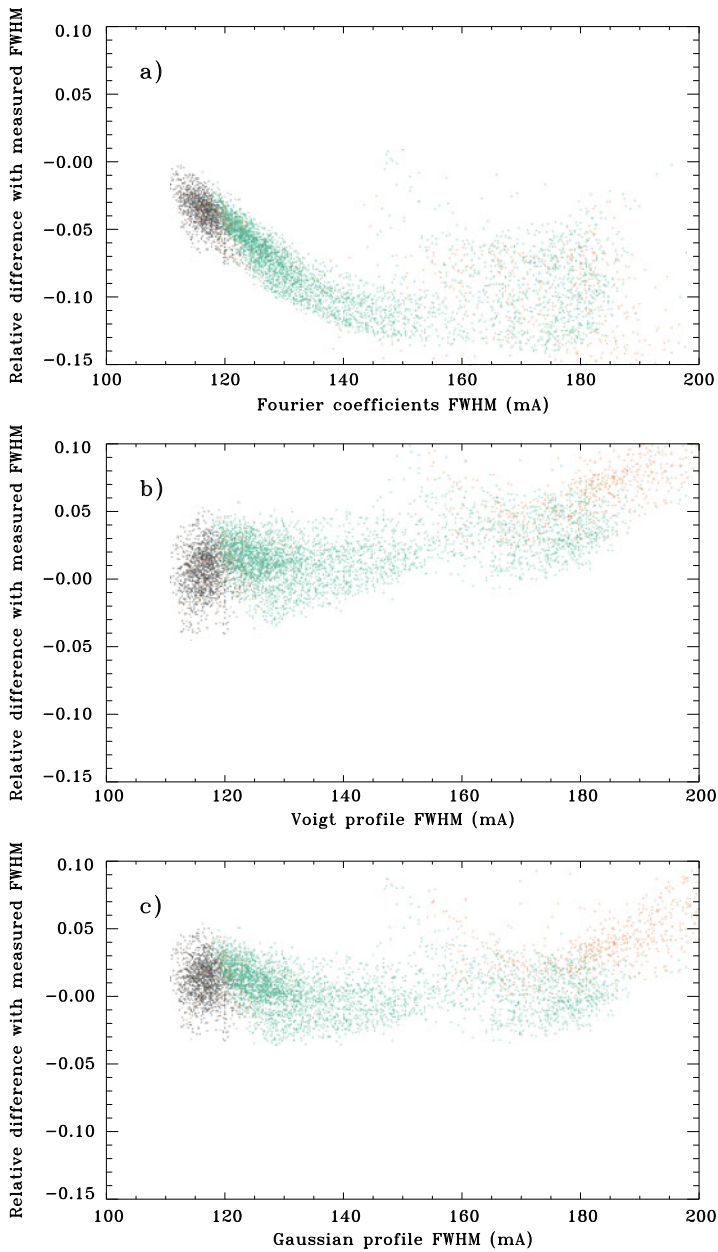
Figure 15 Relative difference in the FWHMs returned by different algorithms with the actual (measured) FWHMs. (a) MDI-like algorithm; (b) least-squares fit with a Voigt profile; (c) least-squares fit with a Gaussian profile. The black dots show pixels for which the absolute magnetic-field strength is < 50 G, the orange dots are for fields > 1600 G, and the green dots are for fields in the range $1000 – 1600$ G.
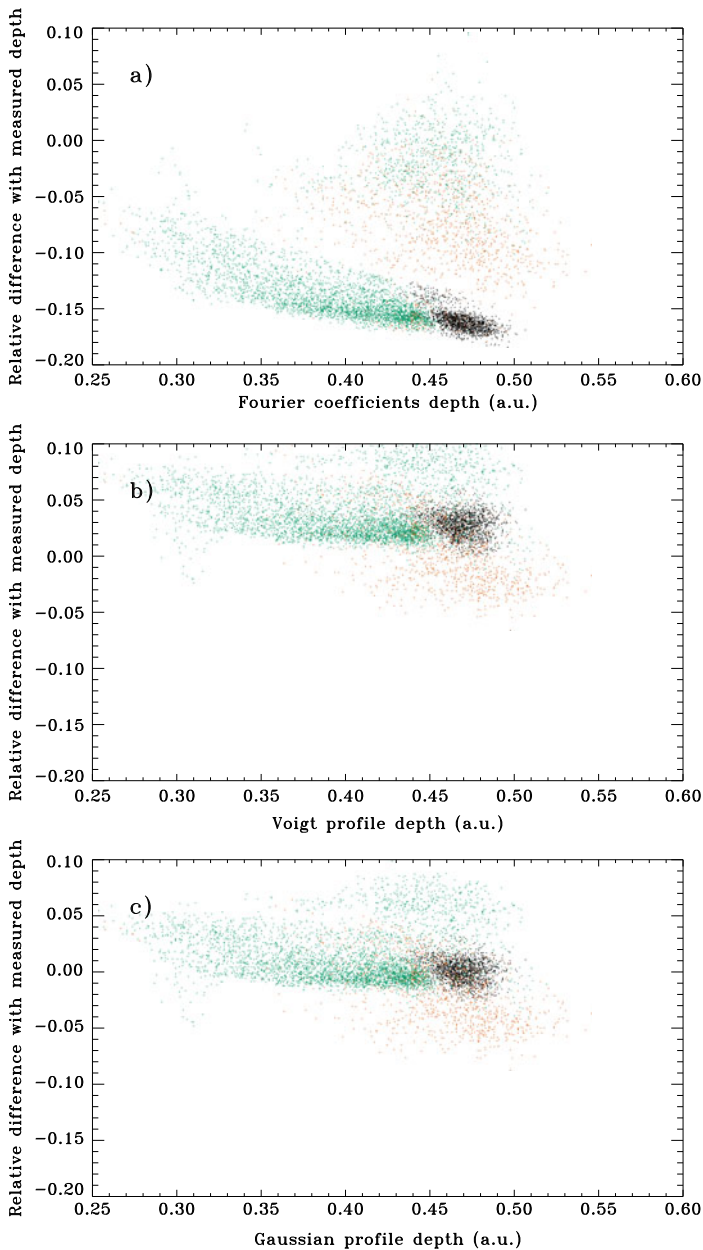
Figure 16 Relative difference in the line depths returned by different algorithms with the actual (measured) line depths. (a) MDI-like algorithm; (b) least-squares fit with a Voigt profile; (c) least-squares fit with a Gaussian profile. The black dots show pixels for which the absolute magnetic field strength is < 50 G, the orange dots are for fields > 1600 G, and the green dots are for fields in the range 1000 – 1600 G.

than might be expected), but it will likely degrade the accuracy of the LOS observables in strong magnetic fields. Instead of trying to improve the MDI-like method, it is probably better to implement a least-squares fit. Despite a few issues, like the computation speed and the occasional lack of convergence, the least-squares fits are more accurate. Although they are slower than the MDI-like algorithm, and their initial guess must be provided by another algorithm, it should be possible to speed up the calculations by linearizing the fit around a realistic iron line profile. In the study on temporally averaged IBIS data, the lack of convergence was an issue only when the initial Doppler velocity guess was set to zero. In that case we encountered non-convergences for a few pixels inside the sunspot. When the initial guess was set to the result of the MDI-like algorithm, the fits converged for all pixels. In the study of simulated Doppler velocities based on three different line profiles (one from an umbral pixel, one from a penumbral pixel, and one from a quiet Sun pixel), we had non-convergences – despite using the appropriate initial guess – only 0.5% of the time and for very large Doppler velocities (> 8500 m s^{-1}). Therefore, for strong sunspots observed by HMI far from solar disk center and at a large Sun–SDO radial velocity, it is quite possible that a least-squares fit does not converge for some pixels.

In the quiet Sun at least, the noise level on Doppler velocities due to photon noise is lower with least-squares fits than with MDI-like algorithms.

Overall, the (first Fourier-coefficients) MDI-like algorithm performs relatively well even in the presence of a strong field. Line widths, line depths, and LOS magnetic field strengths (in absolute value) are underestimated in the sunspot. The line width is underestimated by $\approx 3.9\%$ in the quiet Sun, and by an average $\approx 17.5\%$ in the sunspot, where the field is stronger than 1600 G (in absolute value). The line depth is underestimated by $\approx 16\%$ in the quiet Sun, and by less in the sunspot. The continuum intensity is only slightly underestimated by $1 - 1.7\%$. The absolute value of the LOS field strength is underestimated by an average of $\approx 17\%$ in the sunspot umbra. Finally, the Doppler velocities returned by the first Fourier-coefficients algorithm and the least-squares fits differ by about 90 m s^{-1} (on average) in the sunspot umbra, with a peak difference of ≈ 300 m s^{-1}, after the respective average velocities in the quiet Sun are subtracted from the results of each algorithm.

The results presented here make it possible to partly correct some LOS observables obtained with the current HMI pipeline. For instance, the K_1 and K_2 factors multiplying line width and line depth could be revised upward, and could be a function of the magnetic field strength returned by the MDI-like algorithm. Since the IBIS data were taken prior to the SDO launch, it will be interesting to have simultaneous observations by HMI and IBIS, and to this end a proposal was submitted to – and accepted by – the National Solar Observatory. Finally, the Fe I line seen by IBIS is slightly different from the HMI one (both instruments have different spatial resolutions and scattered light levels), and the line profiles used here are convolved by the IBIS filter transmittances and are temporally averaged. Therefore, the present results might be somewhat different from what the Fe I line seen by HMI would return.

References

Bell, B., Meltzer, A.: 1959, *Smithson. Contrib. Astrophys.* **3**, 39.

Borrero, J.M., Tomczyk, S., Kubo, M., Socas-Navarro, H., Schou, J., Couvidat, S., Bogart, R.: 2010, *Solar Phys.* doi:10.1007/s11207-010-9515-6.

Cavallini, F.: 2006, *Solar Phys.* **236**, 415.

Couvidat, S., Schou, J., Shine, R.A., Bush, R.I., Miles, J.W., Scherrer, P.H., Rairden, R.L.: 2012, *Solar Phys.* **275**, 285. doi:10.1007/s11207-011-9723-8.

Dravins, D., Lindegren, L., Nordlund, Å.: 1981, *Astron. Astrophys.* **96**, 345.

Fleck, B., Couvidat, S., Straus, T.: 2011, *Solar Phys.* **271**, 27. doi:10.1007/s11207-011-9783-9.

Norton, A.A., Graham, J.P., Ulrich, R.K., Schou, J., Tomczyk, S., Liu, Y., Lites, B.W., Lopez Ariste, A., Bush, R.I., Socas-Navarro, H., Scherrer, P.H.: 2006, *Solar Phys.* **239**, 69.

Rajaguru, S.P., Wachter, R., Sankarasubramanian, K., Couvidat, S.: 2010, *Astrophys. J.* **721**, L86.

Scherrer, P.H., Bogart, R.S., Bush, R.I., Hoeksema, J.T., Kosovichev, A.G., Schou, J., *et al.*: 1995, *Solar Phys.* **162**, 129.

Schou, J., Scherrer, P.H., Bush, R.I., Wachter, R., Couvidat, S., Rabello-Soares, M.C., *et al.*: 2012, *Solar Phys.* **275**, 229. doi:10.1007/s11207-011-9842-2.

Skumanich, A., Lites, B.W.: 1987, *Astrophys. J.* **322**, 473.